$\mathcal{R}$esearch in
$\mathcal{A}$stronomy and
$\mathcal{A}$strophysics

In search of infall motion in molecular clumps II: HCO$^+$ (1–0) and HCN (1–0) observations toward a sub-sample of infall candidates

Yang Yang (杨旸)[1,2], Zhi-Bo Jiang (江治波)[1,2,3], Zhi-Wei Chen (陈志维)[1], Shao-Bo Zhang (张少博)[1] , Shu-Ling Yu (于书岭)[1,2] and Yi-Ping Ao (敖一平)[1]

[1] Purple Mountain Observatory, Chinese Academy of Sciences, Nanjing 210008, China; *zbjiang@pmo.ac.cn*
[2] University of Science and Technology of China, Chinese Academy of Sciences, Hefei 230026, China
[3] Center astronomy and Space Sciences, China Three Gorges University, Yichang 443002, China

Abstract Gravitational accretion accumulates the original mass. This process is crucial for us to understand the initial phases of star formation. Using the specific infall profiles in optically thick and thin lines, we searched the clumps with infall motion from the Milky Way Imaging Scroll Painting (MWISP) CO data in previous work. In this study, we selected 133 sources as a sub-sample for further research and identification. The excitation temperatures of these sources are between 7.0 and 38.5 K, while the H$_2$ column densities are between 10^{21} and 10^{23} cm^{-2}. We have observed optically thick lines HCO$^+$ (1–0) and HCN (1–0) using the DLH 13.7-m telescope, and found 56 sources with a blue profile and no red profile in these two lines, which are likely to have infall motions, with a detection rate of 42%. This suggests that using CO data to restrict the sample can effectively improve the infall detection rate. Among these confirmed infall sources are 43 associated with Class 0/I young stellar objects (YSOs), and 13 which are not. These 13 sources are probably associated with the sources in the earlier evolutionary stage. In comparison, the confirmed sources that are associated with Class 0/I YSOs have higher excitation temperatures and column densities, while the other sources are colder and have lower column densities. Most infall velocities of the sources that we confirmed are between 10^{-1} to 10^0 km s^{-1}, which is consistent with previous studies.

Key words: stars: formation — ISM: kinematics and dynamics — ISM: molecules — radio lines: ISM

1 INTRODUCTION

The study of star formation shows that stars form through inside-out gravitational collapse in dense molecular clumps (Shu et al. 1987), while the accretion flow is maintained in the subsequent evolutionary processes to feed the forming stars. Gravitational infall mainly occurs in Class 0/I young stellar objects (YSOs) (Bachiller 1996). These sources are at the beginning stages of their evolution, and their emissions are dominated by the infalling envelopes (e.g., Allen et al. 2004). After Class II stage, the infall motion no longer dominates. Therefore, the research on infall motion helps us to better understand the physical process of the initial stage of star formation.

According to the model of infalling clumps (e.g., Leung & Brown 1977), a pair of optically thick and thin lines can be used as a tracer for infall motion. The optically thick line will self-absorb when passing through the clumps. When the gas falls into the core, the line will produce a Doppler shift along the line of sight. This causes the

self-absorption of the optically thick line to shift slightly to the red. In this case, the line produces a double-peaked profile with the blue peak stronger than the red one. If the self-absorption is weak, then the red peak may not be so obvious, and the line will show a blue peak profile with a red shoulder, or a single-peaked profile with the peak skewed to the blue. This kind of feature is commonly referred to as a blue profile. Meanwhile, the optically thin line shows a single-peaked profile, with the peak between the double-peaks of the optically thick line. If the optically thick line shows a single peak, then the peak of optically thin line is slightly skewed to the red in comparison. The velocity of optically thin line can be used to indicate the central radial velocity. Therefore, an optically thin line is a good way to distinguish between self-absorption and multiple components. In recent years, using this method, a number of researches have been conducted on the infall motion (e.g., He et al. 2015; Calahan et al. 2018; Saral et al. 2018), but most of them have focused on known star-forming regions.

If we are able to obtain an unbiased large-scale infall sample in the Milky Way, then we may estimate the number of clumps with infall motion, which will help us to infer the lifetime of infall.

Instead of looking for infall candidates in known star-forming regions, we use the Milky Way Imaging Scroll Painting (MWISP) data by the DLH 13.7-m telescope to search the infall candidates in the Galactic disk. The MWISP project provides $^{12}CO\,(1–0)$ and its isotopes $^{13}CO\,(1–0)$ and $C^{18}O\,(1–0)$. These three lines can be used as a start to search for infall motions in the molecular clumps. Using the combinations of ^{12}CO and ^{13}CO, ^{13}CO and $C^{18}O$, about 2200 candidates were preliminarily identified by blue profiles (Jiang et al. 2020, in prep). We further selected 133 candidates for follow-up study. Compared with CO, HCO$^+$ and HCN are generally optically thick lines, and can trace denser regions, which are believed to be more effective tracers of infall profile (e.g. Vasyunina et al. 2011; Peretto et al. 2013; Yuan et al. 2018; Zhang et al. 2018). In this paper, using the DLH 13.7-m telescope, we carried out HCO$^+$ (1–0) and HCN (1–0) lines observations toward our sub-sample. Based on the observations of these two lines and optically thin line $C^{18}O\,(1–0)$, we further identified our sources. We then discuss the physical properties and infall velocities of the confirmed infall sources.

In Section 2, we briefly introduce our source selection criteria and the observations. The results and discussion based on CO data, and HCO$^+$ and HCN lines analysis are given in Section 3. Finally, a summary is provided in Section 4.

2 THE SAMPLE AND OBSERVATIONS

The MWISP project is an on-going, unbiased CO survey along the Galactic plane in the range of $l = [−10°, 250°]$, $b = [−5.2°, 5.2°]$, observing $^{12}CO\,(1–0)$, $^{13}CO\,(1–0)$, and $C^{18}O\,(1–0)$ lines simultaneously (Su et al. 2019). At present, the project has completed about 80%. Using the combinations of ^{12}CO and ^{13}CO, ^{13}CO and $C^{18}O$, about 2200 candidates showing blue profiles were identified by machine search and manual check up to the end of 2017 (Jiang et al. 2020, in prep). In the first step to confirm these candidates, we selected 133 with significant blue profiles in ^{12}CO, and $C^{18}O$ intensities greater than 1 K as a sub-sample for further study. Table 1 lists the selected sources, where the kinematic distances are calculated by the model from Reid et al. (2014). If the sources have kinematic distance ambiguity (KDA), then the nearer one is chosen.

HCO$^+$ and HCN trace the dense regions in molecular clouds, and they are generally optically thick lines in these regions. Their line profiles can provide some information of gas motions in dense clumps (e.g., Smith et al. 2012). From 2018 May 14 to 25, we carried out

the follow-up single-pointing observations (project code: 18A004) toward the 133 selected sources. The front-end of the telescope is the 3×3 beam sideband-separating Superconducting Spectroscopic Array Receiver (SSAR) (Shan et al. 2012), and we used the spectrum from beam 2 of the array. The back-end is a set of 18 Fast Fourier Transform Spectrometers (FFTSs), which can analyze signals from the upper and lower sidebands (Su et al. 2019). The frequencies of HCO$^+$ (1–0) and HCN (1–0) lines are about 89.2 GHz and 88.6 GHz, respectively. The angular resolution of the telescope is about $62''$, and the main beam efficiency is about 56.8% at these frequencies (Gong et al. 2018). Since each sideband is 1 GHz, we can observe them at the same time. We have observed a total of 102 targets of these two lines. The data of the remaining 31 targets were obtained from the Millimeter Wave Radio Astronomy Database[1] (among them, 14 targets lack HCN data). The data were reduced using the CLASS of the GILDAS package[2]. The baselines of the spectra have been first-order fitted, and the fitting regions are $V_{LSR} \pm 40\ \mathrm{km\,s^{-1}}$ excepted the emission regions. Since the observed lines have different frequencies, their velocity resolutions are also different. We smoothed all the spectra to a spectrometer resolution of $0.2\ \mathrm{km\,s^{-1}}$. The on-source integration time is at least 7 minutes for each source, and the typical system temperatures (T_{sys}) are between 150 to 250 K. For some sources with low altitude or high T_{sys}, we repeated observations until the RMS values of these lines are less than 0.1 K at a resolution of $0.2\ \mathrm{km\,s^{-1}}$. The total observing time is about 53 hours for this project.

3 RESULTS AND DISCUSSION

3.1 Properties of the Sample

3.1.1 Excitation temperature and column density

CO lines are widely used to estimate the excitation temperature and column density of molecular clouds because of their high stability, high abundance, wide distribution and easy measurement. In this paper, we use the optically thick line ^{12}CO to calculate the excitation temperature of the selected sources. Since there is self-absorption in ^{12}CO of our sources, we use Gaussian fitting of the waist and foot portions of the profiles to obtain the expected peak intensity values. We fit each line three times and then select the one with maximum peak value. The peak values derived by this method are sensitive to the choice of the fitting portions. After carefully adjusting the fitting portions, we found that the errors are less than 20% in most cases (Jiang et al. 2020, in prep). The excitation temperature T_{ex}

---

[1] *http://www.radioast.nsdc.cn/*

[2] *http://www.iram.fr/IRAMFR/GILDAS/*

Table 1 The Derived Clump Parameters

Source Name	RA (J2000)	Dec (J2000)	V_{LSR} (km s^{-1})	Distance (kpc)	$T_{ex}(^{12}CO)$ (K)	$\log(N(H_2))$ (cm^{-2})
G002.97+4.22	17:36:36.4	–24:11:31	19.7	4.88	9.5	21.20
G012.34–0.09†	18:12:53.7	–18:17:01	34.2	3.35	14.6	22.25
G012.72+0.69†	18:10:46.9	–17:34:15	17.3	1.94	21.8	22.19
G012.77–0.19†	18:14:08.2	–17:57:04	35.6	3.38	33.0	23.13
G012.82–0.19†	18:14:13.3	–17:54:53	34.9	3.33	38.5	23.61
G012.87–0.20†	18:14:22.1	–17:52:02	35.5	3.36	25.5	23.01
G012.88–0.24†	18:14:32.4	–17:52:48	35.8	3.38	22.3	23.24
G012.96–0.23†	18:14:39.6	–17:48:36	35.2	3.33	17.1	23.07
G013.79–0.23†	18:16:19.5	–17:04:39	38.0	3.39	17.9	22.63
G013.97–0.15†	18:16:22.0	–16:53:02	40.2	3.50	19.9	22.65

Columns are (from left to right) the source name, its equatorial coordinate, its local standard of rest (LSR) velocity, its heliocentric distance, its excitation temperature, and its H_2 column density. †: Source are associated with Class 0/I YSOs. The full table is available in Appendix B.1.

can be estimated by the peak intensity value $T(^{12}CO)$:

$$T_{ex} = \frac{h\nu}{k} \left\{ \ln \left[1 + \left(\frac{kT(^{12}CO)}{h\nu} + \frac{1}{e^{h\nu/kT_{bg}} - 1} \right)^{-1} \right] \right\}^{-1} \tag{1}$$

where $h\nu/k = 5.53$ for $^{12}CO\,(1-0)$, and T_{bg} is cosmic background radiation temperature; i.e., 2.7 K. The uncertainty of T_{ex} may be mainly due to our previous choice of ^{12}CO fitting portion. This makes it difficult to give the error values. We can only estimate that the errors of T_{ex} are less than 20% in most cases. The left panel of Figure 1 shows the distribution of T_{ex}. As can be seen from the figure, the excitation temperature deviates from the normal distribution. The median value of our sources is 12.2 K. About 98% of the sources have an excitation temperature of less than 30 K, and 38 of them have $T_{ex} < 10$ K, which suggests that our sources are mostly cold clumps. The T_{ex} of remaining three sources G012.77–0.19, G012.82–0.19, and G081.72+0.57 are greater than 30 K. These sources may be some hotter molecular clumps.

In addition, we use the $C^{18}O$ column density to estimate the H_2 column density (Sato et al. 1994):

$$N(C^{18}O) = 2.24 \times 10^{14}$$
$$\times \frac{T_{ex}\tau(C^{18}O)\Delta v(C^{18}O)}{1 - e^{-h\nu/kT_{ex}}} \text{ cm}^{-2}, \tag{2}$$

where $h\nu/k = 5.27$ for $C^{18}O\,(1-0)$, $\tau(C^{18}O)$ is the optical depth and $\Delta v(C^{18}O)$ is the FWHM of line profile. The abundance ratio we assume here is $N(H_2)/N(C^{18}O) \approx 7 \times 10^6$ (Warin et al. 1996; Castets & Langer 1995). The uncertainty of $N(H_2)$ may be more difficult to determine due to the uncertainties of T_{ex}, the local thermal equilibrium assumption, and the abundance ratio of $N(H_2)/N(C^{18}O)$. These factors may bring several times of the error to $N(H_2)$ values. As shown in the right panel of Figure 1, the H_2 column densities of our sources are between 10^{21} and 10^{23} cm^{-2}, with the median value of 1.03×10^{22} cm^{-2}. Although the x-axis is in logarithmic

scale, the H_2 column density still seems to deviate from the normal distribution at the high-density end. It may be a power-law distribution at the high-density end.

3.1.2 Association with infrared point sources

In order to better study the star formation status of these 133 sources, we check the association between the infrared point sources and our selected sources. If the infrared point sources located within a radius of $1'$ of our sources, we believe that this source is associated with the infrared point sources. There are 23 sources associated with IRAS point sources (Helou & Walker 1988), and 6 of them are associated with ultracompact HII (UC HII) regions from the criteria by Wood & Churchwell (1989). After excluding the foreground stars, almost all sources are associated with WISE point sources (Wright et al. 2010), and 71 of them are associated with Class 0/I YSOs according to the criteria given by Koenig et al. (2012). For our sources in the Galactic latitudes $|b| \leq 1°$ and longitudes $l = 0 - 65°$, Spitzer GLIMPSE (Benjamin et al. 2003; Churchwell et al. 2009) and MIPSGAL (Gutermuth & Heyer 2015) surveys can also be used to estimate the evolutionary stages empirically. Sixty-four of our sources are associated with GLIMPSE and MIPSGAL point sources. Gutermuth et al. (2008) gave the selected criteria for Class 0/I YSOs. According to this criteria, 60 sources are associated with Class 0/I YSOs. Combined with these infrared point source tables, a total of 94 sources are associated with Class 0/I YSOs, and 6 of them are associated as UC HII regions. The remaining 39 sources are not associated with Class 0/I YSOs. These sources are probably in the early infall stage. The median values of T_{ex} for the sources that are associated with Class 0/I YSOs and not associated with Class 0/I YSOs are 13.3 and 10.5 K, while the corresponding mean values of $N(H_2)$ are 1.43×10^{22} and 6.79×10^{21} cm^{-2}, respectively. Both distributions show that the sources associated
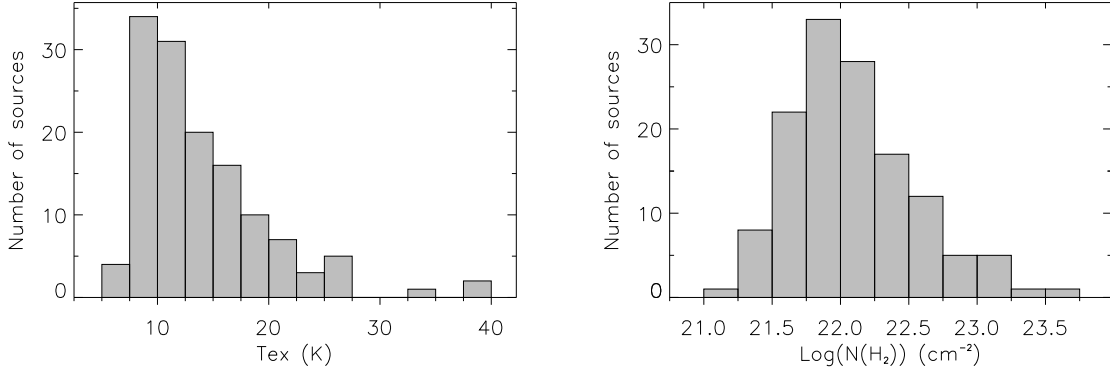
Fig. 1 Distributions of the excitation temperatures and H_2 column densities of 133 sources. *Left panel*: The excitation temperature distribution. *Right panel*: The H_2 column density distribution derived from $C^{18}O$ (1–0).

with Class 0/I YSOs have slightly higher excitation temperatures and column densities.

3.2 HCO$^+$/ HCN Blue-profile Sources

About 80% of our sources show HCO$^+$ (1–0) emissions. Among them, the line profiles of 54 sources are double-peaked profiles and 50 sources are single-peaked profiles. The other three sources show complex line profiles, with three or more peaks, e.g., G045.45+0.05, and we have not classified these line profiles. The hyperfine structure of HCN (1–0) produces complex line profiles. In this paper, we only consider the main peak. Based on the observations, we have found that 82 sources show HCN emissions, with the detection rate of 69%. There are 34 sources with double-peaked profile and 45 sources with single-peaked profile. The remaining sources show complex features in their main peaks and we have not classified their profiles.

Using the dimensionless parameter δV defined by Mardones et al. (1997), we can further quantify the asymmetry of HCO$^+$ and HCN lines:

$$\delta V = \frac{V_{thick} - V_{thin}}{\Delta V_{thin}}, \qquad (3)$$

where V_{thick} and V_{thin} are the peak velocities of optically thick and thin lines, and ΔV_{thin} is the FWHM of the optically thin line. The V_{thick} values are taken from the brightest emission peak positions of HCO$^+$ (1–0) and HCN (1–0) lines, and the V_{thin} and FWHM are taken from the Gaussian fitting of $C^{18}O$ (1–0). The dimensionless parameters δV of HCO$^+$ and HCN lines are given in Table 2, and the statistical distributions are shown in Figure 2. Following the criteria of Mardones et al. (1997) (i.e. sources with $\delta V < -0.25$ are considered to have significant blue profiles, sources with $\delta V > 0.25$ are considered to have significant red profiles, and sources with $-0.25 < \delta V < 0.25$ have neither asymmetry profiles), 52 sources show blue profiles for HCO$^+$ line (31 of them

show double-peaked profiles), while 25 sources show red profiles for this line. For the HCN line, 36 sources show blue profiles (15 of them show double-peaked profiles) and fifteen sources show red profiles. The line profiles of the remaining sources do not show asymmetry. The profile asymmetries are also given in Table 2. Compared to the HCN lines, HCO$^+$ have a higher detection rate and show more line profile asymmetries, suggesting that this line is better for tracing infall motion.

We identify that clumps with infall profile evidence in at least one optically thick line, and no expansion evidence are infall candidates (Gregersen et al. 1997). Therefore, according to the HCO$^+$ and HCN observations given in our study, there are 56 sources meet this criterion and we consider them as confirmed infall sources with higher confidence. Figure 3 shows an example that has significant infall profiles on both HCO$^+$ and HCN lines. The detection rate of the confirmed sources is about 42%. This relatively high detection rate suggests that it is effective to restrict sample with CO data from the MWISP project. Among these confirmed sources, 43 sources are associated with Class 0/I YSOs (three of them are associated with UC HII regions), accounting for 77% of all confirmed sources. The remaining 13 sources are not associated with Class 0/I YSOs.

3.3 Physical Properties of the Confirmed Sources

3.3.1 Physical properties

Figure 4 shows the distributions of some physical parameters for the confirmed infall sources with different evolutionary stages. Among them, the red histograms show the distributions of confirmed sources which are associated with Class 0/I YSOs. The blue histograms show the distributions of the confirmed sources which are not associated with Class 0/I YSOs, and these confirmed sources
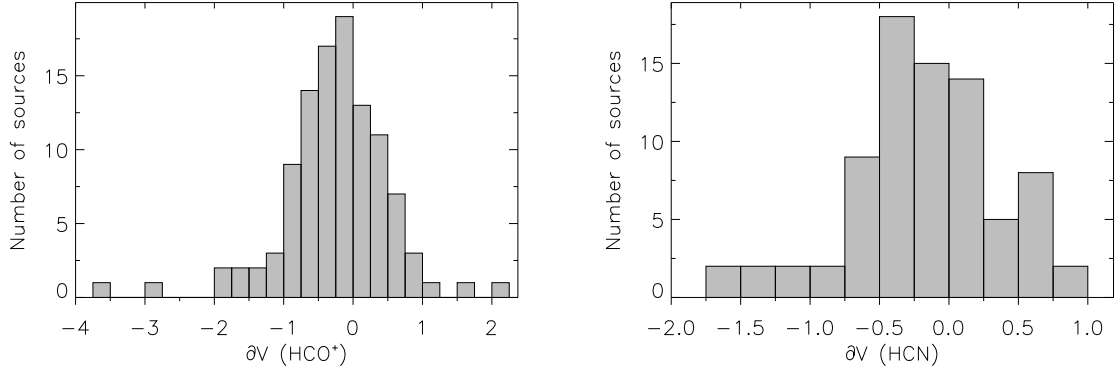
Fig. 2 The dimensionless parameter δV of HCO$^+$ (1–0) and HCN (1–0) of the detected sources. *Left panel*: The δV distribution of HCO$^+$ (1–0) of our sources. *Right panel*: The δV distribution of HCN (1–0) of our sources.

Table 2 The Derived Line Parameters and Profiles of Sample

Source Name	$V_{\rm thick}$ HCO$^+$ (1–0) (km s^{-1})	$V_{\rm thick}$ HCN (1–0) (km s^{-1})	$V_{\rm thin}$ C^{18}O (1–0) (km s^{-1})	ΔV C^{18}O (1–0) (km s^{-1})	δV HCO$^+$ (1–0)	δV HCN (1–0)	Profile
G002.97+4.22	-	19.25(0.19)	19.67(0.02)	0.24(0.01)	-	–1.75(0.79)	N,B
G012.34–0.09	-	-	34.34(0.05)	2.51(0.11)	-	-	N,N
G012.72+0.69	16.70(0.09)	17.26(0.26)	17.28(0.04)	1.66(0.08)	–0.35(0.05)	–0.01(0.15)	B,N $^\alpha$
G012.77–0.19	33.42(0.20)	35.16(0.20)	35.78(0.02)	3.90(0.05)	–0.61(0.05)	–0.16(0.05)	B,N
G012.82–0.19	34.69(0.04)	34.68(0.06)	34.94(0.01)	4.52(0.02)	–0.06(0.01)	–0.06(0.01)	N,N
G012.87–0.20	34.90(0.37)	34.32(0.20)	35.42(0.03)	4.41(0.06)	–0.12(0.08)	–0.25(0.05)	N,B
G012.88–0.24	38.17(0.03)	No data	35.90(0.01)	3.94(0.03)	0.58(0.01)	No data	R
G012.96–0.23	32.20(0.14)	No data	35.23(0.02)	4.87(0.05)	–0.62(0.03)	No data	B $^{\alpha,\beta}$
G013.79–0.23	38.81(0.06)	38.59(0.11)	38.01(0.02)	2.30(0.05)	0.35(0.03)	0.25(0.05)	R,R
G013.97–0.15	37.97(0.12)	37.82(0.13)	39.66(0.03)	3.18(0.07)	–0.53(0.04)	–0.58(0.04)	B,B $^\alpha$

Columns are (from left to right) the source name, peak velocity of HCO$^+$ (1–0), peak velocity of HCN (1–0), peak velocity of C^{18}O (1–0), FWHM of C^{18}O (1–0), asymmetry of HCO$^+$ (1–0), asymmetry of HCN (1–0), and profile of HCO$^+$ (1–0) and HCN (1–0). The values in parentheses give the uncertainties. The HCO$^+$ (1–0) and HCN (1–0) profiles are evaluated: B denotes blue profile, R denotes red profile, and N denotes either non-detection or detection with a single symmetric peak. $^{\alpha,\beta,\gamma}$ indicates a source which are associated with the ATLASGAL compact sources, the ATLASGAL cold high-mass clumps, and the BGPS sources. The full table is available in Appendix B.2.

may be in the earlier evolutionary stage. For all confirmed sources, their excitation temperatures are between 8.7 and 33.0 K, with a median value of 14.4 K. The distribution still deviates from the normal distribution, and is not much different from the $T_{\rm ex}$ distribution of 133 sources. The H$_2$ column density shows an approximately normal distribution when the x-axis is a logarithmic scale, with the median value of 1.67×10^{22} cm^{-2}. For confirmed sources of different evolutionary stages, the confirmed sources associated with Class 0/I YSOs have significantly higher $T_{\rm ex}$ and H$_2$ column densities. Those sources that are not associated with Class 0/I YSOs are mostly cold, and their H$_2$ column densities are less than the median value of all confirmed sources.

Among the 56 confirmed sources, six (i.e., G014.25–0.17, G025.82–0.18, G028.20–0.07, G029.60–0.63, G037.05–0.03 and G049.07–0.33) are associated with the APEX Telescope Large Area Survey of the Galaxy (ATLASGAL) cold high-mass clumps (Wienen et al. 2012), of which G025.82–0.18, G028.20–0.07, G029.60–

0.63, and G049.07–0.33 are also associated with ATLASGAL compact sources (Contreras et al. 2013; Urquhart et al. 2014). In addition, eight confirmed sources are only associated with the ATLASGAL compact sources. The excitation temperatures of these sources are about 10 to 20 Kelvin, and the median value is 17.3 K, which is slightly higher than the median value of all 56 confirmed sources. These sources have relatively high hydrogen column densities, and about 78% of them have a column density higher than the median value of all confirmed sources. In addition, there are 21 sources associated with the Bolocam Galactic Plane Survey (BGPS) sources (Ginsburg et al. 2013). The coordinates of these BGPS sources are within a radius of 1$'$ of our sources, and the central radial velocities differ by less than 3 km s^{-1}. The distributions of the physical properties of these sources are similar to the distributions of all confirmed sources, except that their median values of excitation temperature and column density are slightly higher than the confirmed sources.
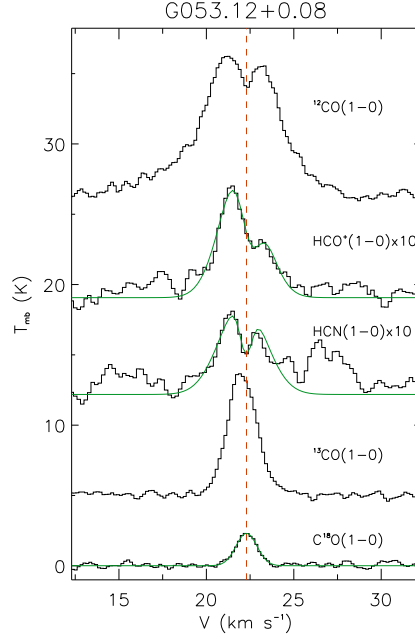
Fig. 3 Example of the confirmed infall sources G053.12+0.08. The lines from bottom to top are $C^{18}O\,(1\text{–}0)$, $^{13}CO\,(1\text{–}0)$, $HCN\,(1\text{–}0)$, $HCO^+\,(1\text{–}0)$ and $^{12}CO\,(1\text{–}0)$, respectively. The *green lines* are the results of Gaussian fitting of $C^{18}O\,(1\text{–}0)$, $HCO^+\,(1\text{–}0)$ and $HCN\,(1\text{–}0)$ lines, and the *dashed red line* indicates the central radial velocity of $C^{18}O\,(1\text{–}0)$.
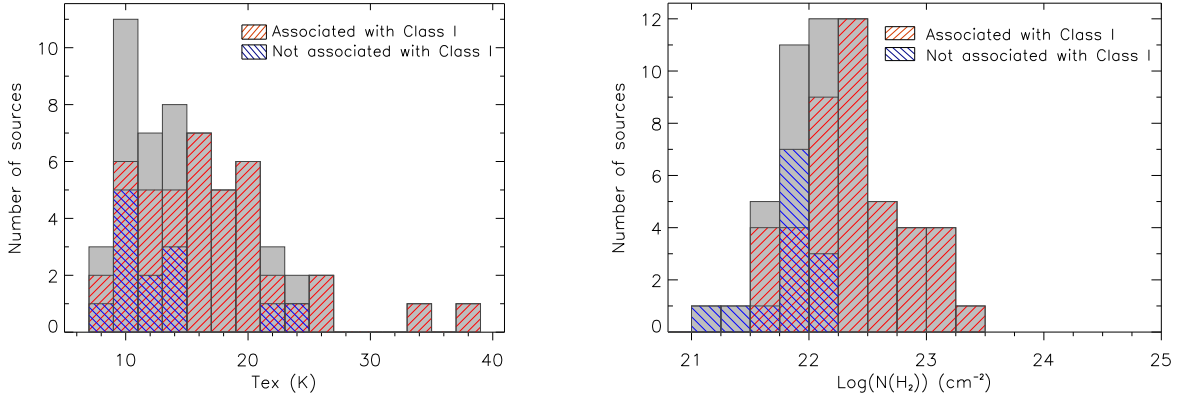
Fig. 4 Distributions of the excitation temperatures and H_2 column densities for confirmed sources. Left panel: The excitation temperature T_{ex} distribution for all confirmed sources (*gray histogram*), the confirmed sources associated with Class 0/I YSOs (*red histogram*) and not associated with Class 0/I YSOs (*blue histogram*). Right panel: The H_2 column densities for all confirmed sources (*gray histogram*), the confirmed sources are associated with Class 0/I YSOs (*red histogram*) and not associated with Class 0/I YSOs (*blue histogram*).

3.3.2 Infall velocities

Myers et al. (1996) gave a method to estimate the infall velocity of clumps based on their model and the assumption of $V_{\mathrm{in}} \ll \Delta V_{\mathrm{thin}}(2\ln\tau)^{1/2}$:

$$V_{\mathrm{in}} = \frac{\Delta V_{\mathrm{thin}}^2}{V_{\mathrm{red}} - V_{\mathrm{blue}}} \ln\left(\frac{1 + e^{(T_{\mathrm{blue}} - T_{\mathrm{dip}})/T_{\mathrm{dip}}}}{1 + e^{(T_{\mathrm{red}} - T_{\mathrm{dip}})/T_{\mathrm{dip}}}}\right), \quad (4)$$

where V_{red} and V_{blue} are the velocities of the red and blue peaks of optically thick line, while T_{red} and T_{blue} are the corresponding peak intensities. T_{dip} is the intensity of self-absorption dip between the two peaks, and ΔV_{thin} is the same as in Section 3.2. Since the above formula contains the velocities and peak intensities corresponding to the blue and red peaks of the optically thick lines, the confirmed sources with the double-peaked profile can use this

Table 3 Infall Velocities of Confirmed Infall Sources with Double-peaked HCO$^+$ (1–0) Profile

Source Name	V_{in} (km s^{-1})	Source Name	V_{in} (km s^{-1})
G012.72+0.69	0.24(0.22)	G053.11+0.09	1.03(0.64)
G012.87–0.20	2.02(1.37)	G053.12+0.08	0.64(0.21)
G012.96–0.23	11.22(7.04)	G053.14+0.09	0.19(0.13)
G013.97–0.15	0.49(0.12)	G079.24+0.53	3.92(3.75)
G014.02–0.19	2.50(0.62)	G079.71+0.15	0.68(0.57)
G014.11–0.16	1.88(1.54)	G081.72+0.57	5.38(0.21)
G014.26–0.17	2.44(2.01)	G081.72+1.28	0.91(0.20)
G017.09+0.82	0.20(0.06)	G081.90+1.43	0.11(0.04)
G025.82–0.18	8.49(1.51)	G082.17+0.07	0.08(0.02)
G026.32–0.07	6.71(6.13)	G085.05-1.25	2.29(0.70)
G028.20–0.07	0.36(0.03)	G108.99+2.73	0.88(0.23)
G028.97+3.54	2.43(0.32)	G110.32+2.52	0.43(0.25)
G029.60–0.63	9.84(3.20)	G110.32+2.54	0.01(0.01)
G036.02–1.36	1.44(1.19)	G121.31+0.64	1.63(0.40)
G039.45–1.17	0.35(0.19)	G172.77+2.09	0.22(0.11)
G053.10+0.11	0.49(0.18)		

Columns are (from left to right) the source name, its infall velocity, the source name, and its infall velocity. The values in parentheses give the uncertainties.
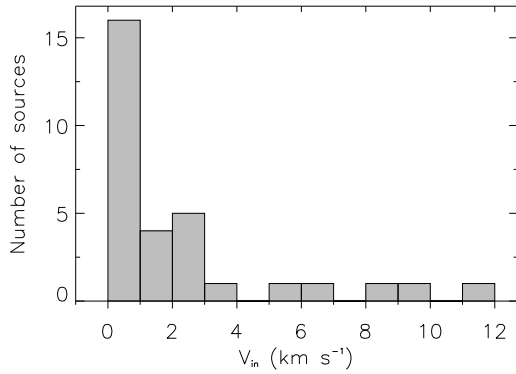
Fig. 5 Distribution of infall velocities for 31 confirmed sources with double-peaked profile in HCO$^+$ (1–0).

formula to calculate the infall velocities. Observations suggest that HCO$^+$ lines show more double-peaked profiles (see Sect. 3.2) than the HCN lines, so we estimated the infall velocities of 31 confirmed sources with double-peaked HCO$^+$ line profiles. The obtained V_{in} values are listed in Table 3, and Figure 5 shows its distribution. In previous studies, the infall velocities of the host clumps were about 10^{-1} to 10^0 km s^{-1} (e.g., Rygl et al. 2013; Qin et al. 2016). Most of our results fall within this range, with the median value of 0.91 km s^{-1}. However, some of the V_{in} we calculated are lager than expected. For example G012.96–0.23, its calculated infall velocity reached 11.22 km s^{-1}, and the error was quite high. We analyzed the above formula and found that the second item on the right has a large influence on the V_{in} value. When the signal-to-noise ratio is not large enough, the noise is likely to cause a large deviation in T_{dip} and even T_{red} values. This will affect the estimation of the infall velocity. Another reason may be

that these sources are not satisfy the assumption given by this model.

We also tried to calculate the mass infall rates of these sources using V_{in}, but we lack the mapping data, only the C^{18}O integrated intensity data can be used to estimate the sizes of clumps. According to previous studies, for low-mass star formation, the mass infall rates onto the host clumps are about 10^{-5} to 10^{-6} $M_\odot$ yr^{-1} (e.g., Palla & Stahler 1993; Whitney et al. 1997; Kirk et al. 2005). For the massive star formation, the rates are between 10^{-2} to 10^{-4} $M_\odot$ yr^{-1} (e.g., Rygl et al. 2013; He et al. 2015). Unfortunately, the results we obtained are an order of magnitude larger than the values given in these studies. Our estimation of the clump sizes are very simple and may be the cause of excessive mass infall rates. Future higher resolution mapping observations may limit the infall scale, and help us to obtain more reliable mass infall rates.

4 SUMMARY

In the previous work, using the CO data from the MWISP project, approximately 2200 candidates with infall spectral characteristics were identified by machine search and manual checking. We selected 133 sources of them with significant blue profiles in ^{12}CO, and C^{18}O intensities > 1 K as a sub-sample for further study. Using the DLH 13.7-m telescope, we carried out observations of optically thick lines HCO$^+$ (1–0) and HCN (1–0) toward these sources. The results are summarized as follows:

(i) There are 107 sources showing HCO$^+$ emission and 82 sources showing HCN emission, with the detection rates of 80% and 69%, respectively. Using the dimensionless parameter δV to quantify the line profile asymmetry, we have found that 52 sources show blue profiles and 25 sources show red profiles in the HCO$^+$ lines, while 36

sources show blue profiles and 15 sources show red profiles in the HCN lines. By comparison, HCO$^+$ lines have a higher detection rate and show more line profile asymmetries.

(ii) Taking the observations of HCO$^+$ and HCN into account, we have identified 56 sources, which may be more reliable infall sources. The detection rate reached 42%, which suggests that our source selection criteria of CO data play an effective role in improving the detection rate of infall motion.

(iii) The excitation temperatures of these 56 confirmed infall sources are between 8.7 and 33.0 K, with a median value of 14.4 K, and the distribution deviates from the normal distribution. When the x-axis is a logarithmic scale, the H$_2$ column density shows a normal distribution, and the median value is 1.67×10^{22} cm^{-2}.

(iv) Of these sources, 43 are associated with Class 0/I YSOs, which have higher excitation temperatures and column densities, accounting for 77% of the sub-sample. The remaining 13 sources are not associated with Class 0/I YSOs. These confirmed sources may be in the early infall stage.

(v) For the confirmed sources with blue double-peaked profile of HCO$^+$ line, we have estimated their infall velocities. Most sources have infall velocities between 10^{-1} to 10^0 km s^{-1}, with the median value of 0.91 km s^{-1}.

In the following work, mapping observations with higher resolution and sensitivity telescope will help us to obtain spatial details of these confirmed sources and further estimate the mass infall rates of the host clumps.

Fig. A.1 Line profiles of 133 sources that we selected. The lines from bottom to top are C^{18}O (1–0), ^{13}CO (1–0), HCN (1–0) (14 sources lack HCN data), HCO$^+$ (1–0) and ^{12}CO (1–0), respectively. The *dashed red line* indicates the central radial velocity of C^{18}O (1–0) estimated by Gaussian fitting. For infall candidates, HCO$^+$ (1–0) and HCN (1–0) lines are also Gaussian fitted. The full figure is *http://www.raa-journal.org/docs/Supp/ms4564TabA1.pdf*.

Table B.1 The Derived Clump Parameters

Source Name	RA (J2000)	Dec (J2000)	V_{LSR} (km s^{-1})	Distance (kpc)	$T_{ex}(^{12}CO)$ (K)	$\log(N(H_2))$ (cm^{-2})
G002.97+4.22	17:36:36.4	–24:11:31	19.7	4.88	9.5	21.20
G012.34–0.09[†]	18:12:53.7	–18:17:01	34.2	3.35	14.6	22.25
G012.72+0.69[†]	18:10:46.9	–17:34:15	17.3	1.94	21.8	22.19
G012.77–0.19[†]	18:14:08.2	–17:57:04	35.6	3.38	33.0	23.13
G012.82–0.19[†]	18:14:13.3	–17:54:53	34.9	3.33	38.5	23.61
G012.87–0.20[†]	18:14:22.1	–17:52:02	35.5	3.36	25.5	23.01
G012.88–0.24[†]	18:14:32.4	–17:52:48	35.8	3.38	22.3	23.24
G012.96–0.23[†]	18:14:39.6	–17:48:36	35.2	3.33	17.1	23.07
G013.79–0.23[†]	18:16:19.5	–17:04:39	38.0	3.39	17.9	22.63
G013.97–0.15[†]	18:16:22.0	–16:53:02	40.2	3.50	19.9	22.65
G014.00–0.13[†]	18:16:22.3	–16:50:48	39.7	3.47	22.3	22.94
G014.02–0.19[†]	18:16:38.2	–16:51:09	40.0	3.48	26.0	22.84
G014.11–0.16[†]	18:16:40.7	–16:45:48	39.1	3.42	16.8	22.44
G014.24–0.50[†]	18:18:12.0	–16:48:29	19.5	2.00	23.3	22.71
G014.25–0.17[†]	18:17:01.3	–16:38:48	38.3	3.36	20.9	22.85
G014.26–0.17[†]	18:17:02.3	–16:38:21	38.5	3.37	19.3	22.80
G014.27–0.51[†]	18:18:16.8	–16:47:24	19.8	2.02	19.9	22.60
G014.42+3.96[†]	18:02:20.4	–14:29:53	29.7	2.78	9.5	22.08
G015.56+2.03	18:11:33.7	–14:26:32	28.9	2.61	10.0	22.01
G016.26+1.00[†]	18:16:41.4	–14:19:16	19.5	1.84	14.9	22.04
G017.09+0.82[†]	18:18:57.2	–13:40:14	22.4	2.01	25.0	22.59
G025.82–0.18[†]	18:39:04.7	–06:24:21	93.7	5.01	17.4	22.75
G026.32–0.07[†]	18:39:36.8	–05:54:42	100.3	5.28	15.0	22.44
G028.20–0.07[†]	18:43:01.8	–04:14:27	97.1	5.19	15.6	22.71
G028.62+4.31	18:28:14.3	–01:51:23	7.7	0.52	7.8	21.83
G028.67+3.68[†]	18:30:32.1	–02:06:24	7.2	0.48	10.1	22.12
G028.67+3.70[†]	18:30:29.5	–02:05:30	7.2	0.48	9.4	22.18
G028.97+3.35[†]	18:32:17.2	–01:59:11	7.3	0.48	12.4	22.37
G028.97+3.36[†]	18:32:14.5	–01:59:24	7.3	0.48	11.7	22.40
G028.97+3.54[†]	18:31:35.4	–01:54:21	7.2	0.48	12.9	22.15
G029.03+4.57[†]	18:28:02.3	–01:22:20	7.3	0.48	8.1	21.99
G029.06+4.58	18:28:03.3	–01:20:46	7.4	0.49	8.7	21.64
G029.18+3.99	18:30:23.2	–01:30:26	8.1	0.54	11.1	22.00
G029.60–0.63[†]	18:47:36.8	–03:15:15	77.2	4.31	13.9	22.56
G029.62+3.19	18:34:02.4	–01:28:57	8.0	0.53	7.7	21.41
G030.17+3.69	18:33:15.2	–00:46:22	9.1	0.61	10.4	21.80
G030.76+2.74[†]	18:37:42.8	–00:40:56	8.1	0.53	8.5	21.68
G031.41+5.24	18:30:00.2	01:02:12	8.3	0.55	13.8	21.99
G031.84+2.57[†]	18:40:17.0	00:12:16	8.6	0.56	8.4	21.96
G033.42+0.00[†]	18:52:20.3	00:26:20	10.6	0.69	8.8	21.60
G033.55+0.29[†]	18:51:31.6	00:40:59	57.6	3.39	7.0	21.83
G034.25+0.16[†]	18:53:16.7	01:14:43	58.1	3.42	19.1	23.28
G034.38+0.22[†]	18:53:18.9	01:23:26	57.5	3.39	11.1	22.53
G034.40+0.21[†]	18:53:22.5	01:24:06	57.3	3.38	10.6	22.32
G035.28+1.31[†]	18:51:04.0	02:41:21	13.1	0.85	7.5	21.40
G036.02–1.36	19:01:55.3	02:07:55	31.8	1.99	10.0	21.93
G036.33–1.27	19:02:11.4	02:26:39	30.4	1.91	7.7	21.74
G036.91–0.43[†]	19:00:14.7	03:20:25	80.2	4.79	10.9	22.17
G036.92+0.71[†]	18:56:12.3	03:52:36	13.0	0.84	7.7	21.70
G036.94+1.09[†]	18:54:52.0	04:03:58	13.2	0.85	7.4	21.60
G037.05–0.03[†]	18:59:04.7	03:38:57	81.3	4.89	13.2	22.51
G037.50+3.05	18:48:53.1	05:27:14	15.5	1.00	9.9	21.39
G038.75–0.97[†]	19:05:31.7	04:43:59	13.2	0.85	9.4	21.31
G039.28–0.19[†]	19:03:44.7	05:33:45	70.5	4.35	11.2	22.35
G039.33–1.02[†]	19:06:48.7	05:13:28	12.8	0.82	8.8	21.75
G039.45–1.17[†]	19:07:32.0	05:15:46	12.7	0.82	8.7	21.58
G039.98+1.67[†]	18:58:23.0	07:02:05	27.8	1.76	10.1	21.72
G040.01–0.94[†]	19:07:45.7	05:51:43	13.5	0.87	9.5	21.84
G044.32–0.79[†]	19:15:16.2	09:45:03	62.1	4.28	10.2	22.06
G045.45+0.05[†]	19:14:22.9	11:08:44	59.3	4.19	20.9	22.74
G048.79+0.02[†]	19:20:54.2	14:05:04	50.1	3.79	12.6	22.14
G049.07–0.33[†]	19:22:42.6	14:09:44	60.4	5.46	19.5	22.48

Table B.1 *Continued.*

Source Name	RA (J2000)	Dec (J2000)	V_{LSR} (km s^{-1})	Distance (kpc)	$T_{\mathrm{ex}}(^{12}\mathrm{CO})$ (K)	$\log(N(\mathrm{H_2}))$ (cm^{-2})
G049.25–1.38	19:26:52.8	13:49:35	5.7	0.39	9.4	21.77
G049.27–1.41	19:27:00.2	13:49:45	5.5	0.37	8.4	21.54
G049.28–1.40	19:27:00.4	13:50:52	5.4	0.37	8.9	21.62
G049.32–1.41	19:27:07.1	13:52:49	5.3	0.36	8.5	21.47
G052.99–0.03[†]	19:29:22.4	17:45:30	22.4	1.68	13.2	21.74
G053.08–0.24[†]	19:30:19.6	17:44:19	23.6	1.78	9.5	21.81
G053.10+0.11[†]	19:29:04.2	17:55:16	22.2	1.67	15.2	21.95
G053.11+0.09[†]	19:29:08.9	17:55:14	22.0	1.65	16.4	22.03
G053.12+0.08[†]	19:29:12.7	17:55:52	22.3	1.68	14.2	22.38
G053.14+0.07[†]	19:29:16.6	17:56:30	22.2	1.67	15.7	22.54
G053.14+0.09[†]	19:29:12.9	17:56:59	22.3	1.68	13.3	22.18
G053.76+0.45[†]	19:29:08.0	18:39:46	23.1	1.77	9.8	21.77
G053.77+0.46[†]	19:29:07.1	18:40:26	23.4	1.79	9.9	21.87
G054.03–2.32[†]	19:39:54.4	17:33:25	17.6	1.33	8.3	21.53
G054.38–0.52[†]	19:33:58.9	18:44:41	34.3	2.87	10.0	21.83
G056.91+3.44	19:24:15.8	22:51:13	11.3	0.92	15.7	21.42
G060.42–0.68[†]	19:47:24.4	23:54:30	29.0	3.57	9.8	21.69
G062.61+1.83	19:42:36.4	27:03:53	2.7	0.29	9.2	21.28
G062.82+1.82	19:43:07.4	27:14:55	2.0	0.23	10.8	21.55
G077.46+1.73	20:20:45.4	39:36:47	1.7	0.63	26.1	22.52
G077.91–1.16	20:34:11.8	38:17:42	–0.5	0.15	14.3	22.19
G079.04+0.64[†]	20:30:10.6	40:16:29	6.6	1.59	25.7	22.38
G079.24+0.53[†]	20:31:15.2	40:22:21	0.3	0.39	10.4	22.41
G079.44+0.18	20:33:21.3	40:19:33	0.1	0.35	9.0	21.89
G079.48+0.25	20:33:12.3	40:23:57	–0.1	0.30	10.0	22.09
G079.71+0.15[†]	20:34:19.9	40:31:12	1.0	0.66	9.1	21.69
G081.04–0.46[†]	20:41:09.8	41:12:47	5.7	1.30	11.1	22.02
G081.62+1.11[†]	20:36:21.1	42:37:18	3.8	1.22	16.7	22.06
G081.69–1.60	20:48:03.4	41:00:48	2.7	1.21	11.9	21.94
G081.72+0.57[†]	20:39:00.7	42:23:07	–3.1	2.56	38.0	23.15
G081.72+1.28	20:35:56.7	42:48:48	3.7	1.20	13.4	22.05
G081.72–1.60[†]	20:48:10.1	41:02:21	2.5	1.20	10.2	21.75
G081.90+1.43	20:35:51.9	43:02:36	11.0	1.18	13.7	21.69
G082.17+0.07[†]	20:42:39.2	42:25:23	10.1	1.14	17.6	22.00
G082.18–1.54	20:49:27.8	41:25:54	2.8	1.13	11.4	21.93
G082.21–1.53[†]	20:49:30.8	41:27:23	2.7	1.13	12.7	22.01
G082.52–1.92	20:52:08.3	41:27:03	4.5	1.09	11.3	21.94
G082.53+0.09[†]	20:43:46.7	42:43:36	9.9	1.08	16.7	22.44
G082.64–1.98	20:52:50.3	41:30:15	4.1	1.07	12.3	21.87
G082.81–2.06	20:53:43.0	41:35:03	4.3	1.04	13.0	22.08
G085.05–1.25[†]	20:58:15.6	43:48:54	–37.5	5.78	9.8	22.05
G085.12+0.50[†]	20:51:00.6	44:59:39	–1.7	1.43	12.2	21.87
G085.47–1.12	20:59:16.8	44:13:06	4.4	0.66	10.5	21.74
G107.50+4.47[†]	22:28:33.3	62:58:29	–2.1	0.00	18.8	22.40
G108.89+2.60[†]	22:46:59.0	62:01:49	–10.3	0.78	17.8	21.99
G108.99+2.73[†]	22:47:13.0	62:11:41	–10.5	0.79	17.4	22.41
G110.32+2.52	22:58:15.9	62:35:29	–12.1	0.90	22.8	22.15
G110.32+2.54	22:58:12.2	62:36:24	–11.9	0.88	24.4	22.22
G110.40+1.67	23:01:58.6	61:50:44	–11.2	0.82	12.6	21.77
G111.12+2.12[†]	23:06:01.2	62:33:12	–9.9	0.68	16.0	22.13
G111.14+2.12[†]	23:06:14.8	62:33:20	–10.0	0.69	13.8	22.05
G111.23+2.07	23:07:07.2	62:33:12	–9.1	0.61	14.6	21.88
G115.62+1.99	23:44:10.6	63:54:14	–10.5	0.65	9.9	21.56
G121.31+0.64[†]	00:36:53.6	63:28:03	–17.3	1.09	16.6	22.24
G121.34+3.42	00:35:40.1	66:14:23	–5.3	0.18	7.2	21.99
G121.35+3.41[†]	00:35:45.3	66:13:55	–5.4	0.19	7.4	21.85
G126.51–1.30[†]	01:21:20.8	61:21:50	–11.7	0.63	11.3	21.73
G126.53–1.17	01:21:40.5	61:29:06	–12.9	0.72	11.9	21.98
G126.67–0.82[†]	01:23:09.2	61:49:29	–13.6	0.77	18.2	22.43
G127.88+2.67[†]	01:38:41.2	65:05:29	–11.5	0.60	13.0	21.98
G133.42+0.00[†]	02:19:51.8	61:03:26	–15.2	0.86	10.6	21.68
G143.04+1.76[†]	03:33:54.9	58:08:19	–8.8	0.42	14.6	21.98
G148.08+0.22[†]	03:55:43.7	53:50:07	–33.7	2.96	9.6	21.83

Table B.1 *Continued.*

Source Name	RA (J2000)	Dec (J2000)	V_{LSR} (km s^{-1})	Distance (kpc)	$T_{ex}(^{12}CO)$ (K)	$\log(N(H_2))$ (cm^{-2})
G154.05+5.08	04:47:13.1	53:03:57	4.3	0.00	10.3	21.49
G172.77+2.09[†]	05:35:50.9	36:10:41	–15.3	5.95	10.9	21.78
G189.67+0.17[†]	06:07:41.5	20:39:44	7.3	2.58	16.8	22.39
G193.01+0.14[†]	06:14:25.2	17:43:20	7.9	1.91	20.4	22.22
G194.73-3.38[†]	06:05:01.0	14:31:04	12.3	2.58	9.9	21.90
G201.16+0.37	06:31:04.4	10:38:12	5.4	0.79	11.4	21.66
G207.58–1.72[†]	06:35:29.7	03:58:31	12.5	1.32	15.0	22.26
G217.30–0.05[†]	06:59:14.3	–03:54:35	26.6	2.34	22.1	22.41

Columns are (from left to right) the source name, its equatorial coordinate, its local standard of rest (LSR) velocity, its heliocentric distance, its excitation temperature, and its H$_2$ column density. [†]: Source are associated with Class 0/I YSOs.

Table B.2 The Derived Line Parameters and Profiles of Sample

Source Name	V_{thick} HCO$^+$ (1-0) (km s^{-1})	V_{thick} HCN (1-0) (km s^{-1})	V_{thin} C^{18}O (1-0) (km s^{-1})	ΔV C^{18}O (1-0) (km s^{-1})	δV HCO$^+$ (1-0)	δV HCN (1-0)	Profile
G002.97+4.22	-	19.25(0.19)	19.67(0.02)	0.24(0.01)	-	–1.75(0.79)	N,B
G012.34–0.09	-	-	34.34(0.05)	2.51(0.11)	-	-	N,N
G012.72+0.69	16.70(0.09)	17.26(0.26)	17.28(0.04)	1.66(0.08)	–0.35(0.05)	–0.01(0.15)	B,N $^\alpha$
G012.77–0.19	33.42(0.20)	35.16(0.20)	35.78(0.02)	3.90(0.05)	–0.61(0.05)	–0.16(0.05)	B,N
G012.82–0.19	34.69(0.04)	34.68(0.06)	34.94(0.01)	4.52(0.02)	–0.06(0.01)	–0.06(0.01)	N,N
G012.87–0.20	34.90(0.37)	34.32(0.20)	35.42(0.03)	4.41(0.06)	–0.12(0.08)	–0.25(0.05)	N,B
G012.88–0.24	38.17(0.03)	No data	35.90(0.01)	3.94(0.03)	0.58(0.01)	No data	R
G012.96–0.23	32.20(0.14)	No data	35.23(0.02)	4.87(0.05)	–0.62(0.03)	No data	B $^{\alpha,\gamma}$
G013.79–0.23	38.81(0.06)	38.59(0.11)	38.01(0.02)	2.30(0.05)	0.35(0.03)	0.25(0.05)	R,R
G013.97–0.15	37.97(0.12)	37.82(0.13)	39.66(0.03)	3.18(0.07)	–0.53(0.04)	–0.58(0.04)	B,B $^\alpha$
G014.00–0.13	42.26(0.03)	No data	39.66(0.02)	2.85(0.04)	0.91(0.01)	No data	R
G014.02–0.19	38.80(0.05)	38.97(0.20)	40.02(0.02)	2.58(0.04)	–0.47(0.02)	–0.41(0.08)	B,B $^\alpha$
G014.11–0.16	37.50(0.31)	38.70(0.16)	38.87(0.04)	2.84(0.09)	–0.48(0.11)	–0.06(0.06)	B,N
G014.24–0.50	-	No data	19.65(0.01)	1.49(0.02)	-	No data	N
G014.25–0.17	35.73(0.13)	No data	38.14(0.02)	3.09(0.05)	–0.78(0.04)	No data	B $^{\beta,\gamma}$
G014.26–0.17	35.90(0.20)	36.86(0.47)	38.38(0.02)	2.92(0.05)	–0.85(0.07)	–0.52(0.16)	B,B
G014.27–0.51	20.59(0.14)	20.18(0.11)	19.79(0.02)	1.81(0.04)	0.44(0.07)	0.22(0.06)	R,N
G014.42+3.96	29.46(0.21)	29.70(0.29)	29.56(0.03)	1.68(0.08)	–0.06(0.13)	0.08(0.17)	N,N
G015.56+2.03	29.05(0.24)	-	28.94(0.02)	1.13(0.05)	0.10(0.21)	-	N,N
G016.26+1.00	19.52(0.18)	-	19.52(0.02)	0.98(0.04)	0.00(0.18)	-	N,N
G017.09+0.82	20.60(0.19)	20.98(0.12)	22.30(0.02)	2.01(0.05)	–0.85(0.09)	–0.66(0.06)	B,B
G025.82–0.18	92.50(0.02)	No data	93.69(0.02)	3.26(0.06)	–0.37(0.01)	No data	B $^{\alpha,\beta,\gamma}$
G026.32–0.07	99.50(0.07)	99.30(0.11)	100.54(0.02)	2.10(0.06)	–0.50(0.03)	–0.59(0.05)	B,B $^{\alpha,\gamma}$
G028.20–0.07	96.30(0.16)	No data	97.31(0.03)	3.94(0.08)	–0.26(0.04)	No data	B $^{\alpha,\beta,\gamma}$
G028.62+4.31	-	-	7.67(0.01)	0.62(0.03)	-	-	N,N
G028.67+3.68	-	-	7.22(0.01)	0.98(0.03)	-	-	N,N
G028.67+3.70	-	-	7.18(0.01)	1.03(0.03)	-	-	N,N
G028.97+3.35	4.14(0.34)	-	7.36(0.01)	1.15(0.03)	–2.80(0.29)	-	B,N
G028.97+3.36	5.72(0.10)	5.71(0.07)	7.28(0.01)	1.25(0.03)	–1.25(0.08)	–1.26(0.06)	B,B
G028.97+3.54	5.00(0.12)	5.63(0.15)	7.14(0.03)	1.66(0.07)	–1.29(0.07)	–0.91(0.09)	B,B
G029.03+4.57	-	-	7.33(0.01)	0.78(0.03)	-	-	N,N
G029.06+4.58	-	-	7.47(0.01)	0.48(0.03)	-	-	N,N
G029.18+3.99	-	-	8.08(0.03)	1.25(0.06)	-	-	N,N
G029.60-0.63	74.60(0.02)	No data	77.11(0.02)	2.55(0.05)	–0.98(0.01)	No data	B $^{\alpha,\beta,\gamma}$
G029.62+3.19	8.76(0.07)	-	8.06(0.01)	0.35(0.03)	2.00(0.19)	-	R,N
G030.17+3.69	8.67(0.52)	8.27(0.12)	9.06(0.02)	0.84(0.05)	–0.46(0.62)	–0.94(0.14)	B,B
G030.76+2.74	8.13(0.12)	-	7.97(0.02)	0.76(0.06)	0.21(0.15)	-	N,N

Table B.2 *Continued.*

Source Name	V_{thick} HCO$^+$ (1-0) (km s^{-1})	V_{thick} HCN (1-0) (km s^{-1})	V_{thin} C^{18}O (1-0) (km s^{-1})	ΔV C^{18}O (1-0) (km s^{-1})	δV HCO$^+$ (1-0)	δV HCN (1-0)	Profile
G031.41+5.24	7.28(0.10)	8.09(0.11)	8.28(0.02)	0.82(0.04)	−1.22(0.13)	−0.23(0.13)	B,N
G031.84+2.57	9.81(0.14)	-	8.48(0.03)	1.18(0.06)	1.13(0.11)	-	R,N
G033.42+0.00	10.04(0.07)	No data	10.60(0.02)	0.55(0.04)	−1.02(0.12)	No data	B $^{\alpha,\gamma}$
G033.55+0.29			57.52(0.03)	1.00(0.06)			N,N
G034.25+0.16	36.32(0.02)	55.67(0.09)	58.34(0.02)	6.21(0.05)	−3.55(0.00)	−0.43(0.01)	B,B $^{\alpha,\gamma}$
G034.38+0.22	60.34(0.13)	54.29(0.11)	57.54(0.03)	2.82(0.06)	0.99(0.04)	−1.15(0.04)	R,B
G034.40+0.21	59.45(0.33)	No data	57.55(0.05)	3.05(0.11)	0.62(0.11)	No data	R
G035.28+1.31	13.11(0.26)	-	13.12(0.02)	0.40(0.04)	−0.02(0.66)	-	N,N
G036.02−1.36	31.20(0.03)	31.43(0.14)	31.74(0.02)	0.90(0.04)	−0.60(0.03)	−0.34(0.16)	B,B
G036.33−1.27	30.79(0.08)	-	30.58(0.02)	0.82(0.06)	0.26(0.10)	-	R,N
G036.91−0.43	77.78(0.23)	81.17(0.06)	80.23(0.02)	1.55(0.06)	−1.58(0.15)	0.61(0.04)	B,R
G036.92+0.71	-	-	12.92(0.02)	0.64(0.04)	-	-	N,N
G036.94+1.09	-	-	13.22(0.02)	0.49(0.04)	-	-	N,N
G037.05−0.03	80.65(0.07)	No data	81.40(0.03)	2.60(0.06)	−0.29(0.03)	No data	B $^{\alpha,\gamma}$
G037.50+3.05	15.49(0.05)	-	15.50(0.01)	0.31(0.03)	−0.03(0.17)	-	N,N
G038.75−0.97	-	-	13.26(0.02)	0.33(0.04)	-	-	N,N
G039.28−0.19	71.50(0.35)	69.93(0.10)	70.84(0.04)	2.70(0.09)	0.24(0.13)	−0.34(0.04)	N,B $^{\gamma}$
G039.33−1.02	12.80(0.11)	-	12.78(0.02)	0.61(0.04)	0.03(0.18)	-	N,N
G039.45−1.17	12.50(0.39)	-	12.71(0.02)	0.58(0.05)	-0.36(0.68)	-	B,N
G039.98+1.67	28.02(0.13)	27.80(0.14)	27.63(0.02)	0.74(0.05)	0.53(0.17)	0.23(0.19)	R,N
G040.01−0.94	-	-	13.59(0.01)	0.64(0.03)	-	-	N,N
G044.32−0.79	60.66(0.34)	62.70(0.13)	61.90(0.03)	1.53(0.07)	−0.81(0.22)	0.52(0.09)	B,R
G045.45+0.05	60.11(0.07)	59.45(0.59)	59.55(0.05)	4.99(0.12)	0.11(0.01)	−0.02(0.12)	N,N
G048.79+0.02	50.70(0.18)	50.08(0.12)	50.10(0.02)	1.05(0.04)	0.57(0.17)	−0.02(0.11)	R,N
G049.07−0.33	59.38(0.20)	-	60.74(0.03)	2.52(0.08)	−0.54(0.08)	-	B,N $^{\alpha,\beta,\gamma}$
G049.25−1.38	-	4.34(0.06)	5.67(0.02)	0.81(0.05)	-	−1.64(0.07)	N,B
G049.27−1.41	-	-	5.51(0.02)	0.44(0.04)	-	-	N,N
G049.28−1.40	-	-	5.50(0.01)	0.44(0.03)	-	-	N,N
G049.32−1.41	-	-	5.50(0.02)	0.42(0.04)	-	-	N,N
G052.99−0.03	22.57(0.14)	22.19(0.21)	22.36(0.01)	0.54(0.03)	0.39(0.25)	−0.31(0.39)	R,B
G053.08−0.24	23.35(0.23)	-	24.09(0.02)	0.75(0.04)	−0.99(0.30)	-	B,N
G053.10+0.11	22.00(0.06)	21.84(0.06)	22.18(0.02)	0.85(0.04)	−0.21(0.07)	−0.40(0.07)	N,B $^{\alpha,\gamma}$
G053.11+0.09	21.80(0.13)	22.36(0.19)	22.14(0.02)	1.12(0.06)	−0.30(0.12)	0.20(0.17)	B,N
G053.12+0.08	21.50(0.12)	21.50(0.20)	22.29(0.01)	1.37(0.03)	−0.58(0.09)	−0.58(0.15)	B,B $^{\gamma}$
G053.14+0.07	21.60(0.09)	No data	22.04(0.02)	2.22(0.05)	−0.20(0.04)	No data	N
G053.14+0.09	21.54(0.08)	21.66(0.13)	22.64(0.02)	1.32(0.05)	−0.83(0.06)	−0.74(0.10)	B,B $^{\gamma}$
G053.76+0.45	-	-	23.14(0.02)	0.71(0.04)	-	-	N,N
G053.77+0.46	-	-	23.22(0.02)	0.77(0.04)	-	-	N,N
G054.03−2.32	17.37(0.09)	17.76(0.06)	17.49(0.02)	0.53(0.05)	−0.23(0.17)	0.51(0.11)	N,R
G054.38−0.52	34.09(0.06)	34.29(0.15)	34.27(0.02)	0.87(0.05)	−0.21(0.07)	0.02(0.17)	N,N
G056.91+3.44	-	11.12(0.02)	10.88(0.02)	0.35(0.04)	-	0.69(0.06)	N,R
G060.42−0.68	-	-	28.99(0.01)	0.53(0.03)	-	-	N,N
G062.61+1.83	3.48(0.09)	-	3.06(0.02)	0.27(0.03)	1.56(0.32)	-	R,N
G062.82+1.82	-	-	1.92(0.02)	0.53(0.05)	-	-	N,N
G077.46+1.73	2.54(0.07)	2.51(0.15)	1.66(0.02)	1.62(0.04)	0.54(0.04)	0.52(0.09)	R,R
G077.91−1.16	−2.86(0.18)	0.71(0.07)	−0.55(0.03)	1.55(0.06)	−1.49(0.11)	0.81(0.05)	B,R
G079.04+0.64	7.40(0.09)	6.95(0.03)	6.83(0.03)	1.71(0.06)	0.33(0.05)	0.07(0.02)	R,N
G079.24+0.53	−0.30(0.13)	-	0.27(0.01)	1.43(0.03)	−0.40(0.09)	-	B,N $^{\gamma}$
G079.44+0.18	0.31(0.07)	0.12(0.06)	0.16(0.02)	0.97(0.05)	0.15(0.07)	−0.04(0.06)	N,N
G079.48+0.25	0.52(0.20)	0.11(0.12)	0.05(0.03)	1.61(0.07)	0.29(0.12)	0.04(0.07)	R,N
G079.71+0.15	0.60(0.11)	0.79(0.09)	0.97(0.02)	0.65(0.04)	−0.57(0.17)	−0.28(0.14)	B,B $^{\gamma}$
G081.04−0.46	6.08(0.07)	5.87(0.06)	5.66(0.02)	1.04(0.04)	0.40(0.07)	0.20(0.06)	R,N
G081.62+1.11	3.97(0.06)	3.64(0.04)	3.65(0.03)	1.50(0.08)	0.21(0.04)	−0.01(0.02)	N,N
G081.69−1.60	2.87(0.05)	2.71(0.11)	2.64(0.02)	0.82(0.04)	0.28(0.06)	0.09(0.13)	R,N
G081.72+0.57	−5.10(0.03)	No data	−2.83(0.02)	3.31(0.04)	−0.69(0.01)	No data	B $^{\gamma}$
G081.72+1.28	2.90(0.06)	3.50(0.15)	3.84(0.03)	1.31(0.06)	−0.72(0.05)	−0.26(0.11)	B,B
G081.72−1.60	2.90(0.07)	-	2.75(0.03)	0.88(0.06)	0.17(0.08)	-	N,N
G081.90+1.43	10.00(0.13)	10.39(0.20)	11.06(0.02)	0.60(0.01)	−1.77(0.22)	−1.12(0.34)	B,B
G082.17+0.07	9.70(0.55)	8.49(0.14)	10.00(0.02)	1.05(0.06)	−0.29(0.52)	−1.44(0.13)	B,B
G082.18−1.54	2.78(0.07)	2.56(0.13)	2.87(0.01)	0.74(0.03)	−0.12(0.09)	−0.42(0.18)	N,B
G082.21−1.53	2.50(0.05)	2.30(0.14)	2.65(0.01)	0.73(0.03)	−0.21(0.07)	−0.48(0.19)	N,B
G082.52−1.92	4.11(0.20)	4.91(0.05)	4.55(0.01)	0.69(0.03)	−0.64(0.29)	0.52(0.07)	B,R
G082.53+0.09	10.47(0.10)	11.30(0.14)	9.79(0.02)	1.91(0.05)	0.36(0.05)	0.79(0.07)	R,R
G082.64−1.98	3.85(0.09)	5.13(0.14)	4.52(0.02)	0.83(0.05)	−0.81(0.11)	0.73(0.17)	B,R
G082.81−2.06	4.68(0.04)	4.67(0.03)	4.48(0.02)	1.27(0.05)	0.16(0.03)	0.15(0.03)	N,N

Table B.2 *Continued.*

Source Name	V_{thick} HCO$^+$ (1-0) (km s^{-1})	V_{thick} HCN (1-0) (km s^{-1})	V_{thin} C^{18}O (1-0) (km s^{-1})	ΔV C^{18}O (1-0) (km s^{-1})	δV HCO$^+$ (1-0)	δV HCN (1-0)	Profile
G085.05–1.25	–38.90(0.22)	–38.48(0.13)	–37.49(0.04)	1.73(0.08)	–0.82(0.13)	–0.57(0.07)	B,B
G085.12+0.50	-	-	–1.67(0.02)	0.78(0.04)	-	-	N,N
G085.47–1.12	4.81(0.09)	-	4.39(0.01)	0.52(0.03)	0.81(0.17)	-	R,N
G107.50+4.47	–2.90(0.02)	–2.94(0.04)	–2.08(0.02)	1.76(0.05)	–0.47(0.01)	–0.49(0.02)	B,B
G108.89+2.60	–10.27(0.01)	–10.31(0.02)	–10.27(0.02)	0.83(0.04)	0.00(0.02)	–0.05(0.02)	N,N
G108.99+2.73	–11.10(0.05)	–11.08(0.10)	–10.46(0.02)	1.47(0.04)	–0.44(0.03)	–0.42(0.07)	B,B $^\gamma$
G110.32+2.52	–12.90(0.13)	–12.48(0.20)	–12.04(0.02)	1.18(0.06)	–0.73(0.11)	–0.37(0.17)	B,B
G110.32+2.54	–12.50(0.16)	–12.27(0.12)	–11.83(0.02)	1.05(0.04)	–0.64(0.15)	–0.42(0.11)	B,B $^\gamma$
G110.40+1.67	–12.42(0.13)	-	–11.17(0.02)	0.80(0.05)	–1.56(0.16)	-	B,N
G111.12+2.12	–9.87(0.04)	–9.67(0.03)	–9.76(0.02)	1.30(0.06)	–0.08(0.03)	0.07(0.03)	N,N
G111.14+2.12	–9.76(0.09)	–9.59(0.20)	–9.80(0.03)	1.43(0.07)	0.03(0.06)	0.15(0.14)	N,N
G111.23+2.07	–8.92(0.15)	–8.91(0.16)	–9.14(0.02)	0.68(0.04)	0.32(0.23)	0.34(0.24)	R,R
G115.62+1.99	-	-	–10.46(0.01)	0.44(0.03)	-	-	N,N
G121.31+0.64	–18.10(0.01)	–18.06(0.01)	–17.05(0.03)	1.68(0.06)	–0.63(0.01)	–0.60(0.01)	B,B
G121.34+3.42	–5.71(0.04)	–5.69(0.09)	–5.31(0.02)	0.85(0.04)	–0.47(0.05)	–0.45(0.10)	B,B
G121.35+3.41	–5.61(0.09)	–5.43(0.08)	–5.41(0.03)	1.10(0.07)	–0.18(0.08)	–0.02(0.08)	N,N
G126.51–1.30	–11.09(0.06)	–11.28(0.22)	–11.64(0.02)	0.74(0.05)	0.74(0.08)	0.49(0.30)	R,R
G126.53–1.17	–13.05(0.05)	–13.08(0.10)	–12.97(0.03)	1.24(0.06)	–0.06(0.04)	–0.09(0.08)	N,N
G126.67–0.82	–13.83(0.04)	No data	–13.68(0.02)	1.74(0.05)	–0.09(0.03)	No data	N
G127.88+2.67	–11.54(0.04)	–11.68(0.04)	–11.49(0.02)	0.89(0.04)	–0.06(0.04)	–0.21(0.05)	N,N
G133.42+0.00	–15.19(0.21)	–15.61(0.09)	–15.19(0.02)	0.71(0.05)	0.00(0.29)	–0.59(0.13)	N,B
G143.04+1.76	–9.02(0.08)	–8.97(0.07)	–8.62(0.03)	1.17(0.06)	–0.34(0.07)	–0.30(0.06)	B,B
G148.08+0.22	-	–33.12(0.26)	–33.68(0.02)	0.95(0.06)	-	0.59(0.27)	N,R
G154.05+5.08	3.74(0.06)	-	4.58(0.02)	0.44(0.04)	–1.91(0.13)	-	B,N
G172.77+2.09	–15.70(0.09)	–15.13(0.30)	–15.15(0.03)	0.89(0.06)	–0.62(0.10)	0.02(0.34)	B,N
G189.67+0.17	7.24(0.08)	6.64(0.20)	7.46(0.03)	2.22(0.07)	–0.10(0.04)	–0.37(0.09)	N,B
G193.01+0.14	7.48(0.01)	7.27(0.02)	7.80(0.04)	1.92(0.09)	–0.17(0.01)	–0.28(0.01)	N,B $^\gamma$
G194.73–3.38	12.65(0.10)	12.40(0.18)	12.29(0.03)	1.24(0.07)	0.29(0.08)	0.09(0.14)	R,N
G201.16+0.37	5.84(0.13)	5.70(0.12)	5.49(0.02)	0.55(0.04)	0.64(0.24)	0.38(0.21)	R,R
G207.58–1.72	11.11(0.20)	12.87(0.08)	12.19(0.04)	2.24(0.09)	–0.48(0.09)	0.30(0.03)	B,R
G217.30–0.05	26.01(0.05)	26.42(0.07)	26.47(0.03)	1.85(0.06)	–0.25(0.03)	–0.03(0.04)	B,N $^\gamma$

Columns are (from left to right) the source name, peak velocity of HCO$^+$ (1–0), peak velocity of HCN (1–0), peak velocity of C^{18}O (1–0), FWHM of C^{18}O (1–0), asymmetry of HCO$^+$ (1–0), asymmetry of HCN (1–0), and profile of HCO$^+$ (1–0) and HCN (1–0). The values in parentheses give the uncertainties. The HCO$^+$ (1–0) and HCN (1–0) profiles are evaluated: B denotes blue profile, R denotes red profile, and N denotes either non-detection or detection with a single symmetric peak. $^{\alpha, \beta, \gamma}$: indicates a source which is associated with the ATLASGAL compact sources, the ATLASGAL cold high-mass clumps, and the BGPS sources, respectively.

Appendix A: OBSERVED SPECTRAL LINE PROFILES OF SOURCES

Appendix B: THE DERIVED PARAMETERS OF SOURCES

References

Allen, L. E., Calvet, N., D'Alessio, P., et al. 2004, ApJS, 154, 363

Bachiller, R. 1996, ARA&A, 34, 111

Benjamin, R. A., Churchwell, E., Babler, B. L., et al. 2003, PASP, 115, 953

Calahan, J. K., Shirley, Y. L., Svoboda, B. E., et al. 2018, ApJ, 862, 63

Castets, A., & Langer, W. D. 1995, A&A, 294, 835

Churchwell, E., Babler, B. L., Meade, M. R., et al. 2009, PASP, 121, 213

Contreras, Y., Schuller, F., Urquhart, J. S., et al. 2013, A&A, 549, A45

Ginsburg, A., Glenn, J., Rosolowsky, E., et al. 2013, ApJS, 208, 14

Gong, Y., Li, G. X., Mao, R. Q., et al. 2018, A&A, 620, A62

Gregersen, E. M., Evans, II, N. J., Zhou, S., & Choi, M. 1997, ApJ, 484, 256

Gutermuth, R. A., & Heyer, M. 2015, AJ, 149, 64

Gutermuth, R. A., Myers, P. C., Megeath, S. T., et al. 2008, ApJ, 674, 336

He, Y.-X., Zhou, J.-J., Esimbek, J., et al. 2015, MNRAS, 450, 1926

Helou, G., & Walker, D. W. 1988, Infrared Astronomical Satellite (IRAS) Catalogs and Atlases, 7, 1

Jiang Z. B., et al. 2020, in prep

Kirk, J. M., Ward-Thompson, D., & André, P. 2005, MNRAS, 360, 1506

Koenig, X. P., Leisawitz, D. T., Benford, D. J., et al. 2012, ApJ, 744, 130

Leung, C. M., & Brown, R. L. 1977, ApJ, 214, L73

Mardones, D., Myers, P. C., Tafalla, M., et al. 1997, ApJ, 489, 719

Myers, P. C., Mardones, D., Tafalla, M., Williams, J. P., & Wilner, D. J. 1996, ApJL, 465, L133

Palla, F., & Stahler, S. W. 1993, ApJ, 418, 414

Peretto, N., Fuller, G. A., Duarte-Cabral, A., et al. 2013, A&A, 555, A112

Qin, S.-L., Schilke, P., Wu, J., et al. 2016, MNRAS, 456, 2681

Reid, M. J., Menten, K. M., Brunthaler, A., et al. 2014, ApJ, 783, 130

Rygl, K. L. J., Wyrowski, F., Schuller, F., & Menten, K. M. 2013, A&A, 549, A5

Saral, G., Audard, M., & Wang, Y. 2018, A&A, 620, A158

Sato, F., Mizuno, A., Nagahama, T., et al. 1994, ApJ, 435, 279

Shan, W., Yang, J., Shi, S., et al. 2012, IEEE Transactions on Terahertz Science and Technology, 2, 593

Shu, F. H., Adams, F. C., & Lizano, S. 1987, ARA&A, 25, 23

Smith, R. J., Shetty, R., Stutz, A. M., & Klessen, R. S. 2012, ApJ, 750, 64

Su, Y., Yang, J., Zhang, S., et al. 2019, ApJS, 240, 9

Urquhart, J. S., Csengeri, T., Wyrowski, F., et al. 2014, A&A, 568, A41

Vasyunina, T., Linz, H., Henning, T., et al. 2011, A&A, 527, A88

Warin, S., Castets, A., Langer, W. D., Wilson, R. W., & Pagani, L. 1996, A&A, 306, 935

Whitney, B. A., Kenyon, S. J., & Gómez, M. 1997, ApJ, 485, 703

Wienen, M., Wyrowski, F., Schuller, F., et al. 2012, A&A, 544, A146

Wood, D. O. S., & Churchwell, E. 1989, ApJS, 69, 831

Wright, E. L., Eisenhardt, P. R. M., Mainzer, A. K., et al. 2010, AJ, 140, 1868

Yuan, J., Li, J.-Z., Wu, Y., et al. 2018, ApJ, 852, 12

Zhang, G.-Y., Xu, J.-L., Vasyunin, A. I., et al. 2018, A&A, 620, A163